UNIVERSITAT DE BARCELONA

A study of the shortwave schemes in the Weather Research and Forecasting model

Alex Montornès Torrecillas

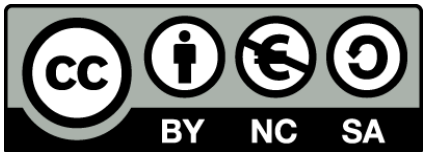

Chapter 5

Study of truncation and TOM errors

In Chapter 4, the different sources of error leading to inaccurate results in modeling the solar radiative transfer have been discussed in Eq. 4.3. As it has been seen, the major limitation for comparing different solar parameterizations is in the model uncertainty and its overlapping with the outcomes of the shortwave scheme. As systematic experiments can not be performed by using the full model from a purely physical point of view, a sandbox tool was presented in Sect. 4.2.1. This tool prepares Dudhia, Goddard, New Goddard, CAM, RRTMG and FLG to be executed with 1-dimensional vertical profiles, which can be provided by ideal or by real conditions.

In this chapter, the sandbox tool is used for analyzing ϵ_{trun} and ϵ_{tom}. In order to perform this kind of study, vertical profiles must be malleable or highly adaptive for testing the schemes under different vertical settings. For this reason, vertical profiles are derived from ideal conditions as it will be described in Sect. 5.1. Moreover, unlike real cases, ideal vertical profiles have the advantage that they allow to enable or disable each atmospheric element such as water vapor or clouds. Thus the contribution of each element to the final result can be analyzed separately.

The disadvantage of this methodology is that the results can not be compared with real measurements and, thus, the physical error can not be evaluated. As a consequence, in this chapter, schemes are assumed as perfect parameterizations and ϵ_{phys} will be neglected from the discussion, leading Eq. 4.3 to

$$\epsilon = \epsilon_{trunc} + \epsilon_{tom}. \tag{5.1}$$

First of all, in Sect. 5.1, the methodology used for these experiments will be presented. The section is divided in two parts. On the one hand, it includes a description of the vertical profiles in Section 5.1.1. On the other hand, the set of experiments designed for the analyses of ϵ_{trunc} and ϵ_{tom} will be detailed in Sect. 5.1.2.

Secondly, the results derived from these experiments are analyzed and discussed in Sects. 5.2 and 5.3. The first one is focused on the analysis of the truncation and TOM errors for the surface irradiances, while the second one offers a full discussion of the physical differences between schemes in surface irradiances as well as fluxes and heating rate profiles. The fact that the solar parameterizations use different approximations will lead to different results that are associated with ϵ_{phys}. These deviations will be used for characterizing the physical aspects of the outcomes.

5.1 Methodology

5.1.1 Ideal vertical profiles

Dry atmosphere

The dry air fields (i.e. temperature T, pressure p and height z) are computed from the ISA of 1976 (National Aeronautics and Space Administration, NASA, 1976), hereinafter denoted as ISA-1976. An ISA is a model that provides an idealized, steady-state representation of how temperature, pressure, density, viscosity, among others vary with height in the Earth's atmosphere, by covering a region from surface to 1000 km. Since the first ISA in 1958, different versions has been released such as the ISA-1962 (NASA, 1962), ISA-1966 (NASA, 1966) and ISA-1976. For the purposes of these experiments, the ISA-1976 (NASA, 1976) has been used because below 32 km is the same that the current model accepted by the International Organization for Standardization, the region with the highest interest for testing the solar schemes.

As it is detailed in the documentation, the ISA-1976 provides two different approaches depending upon the atmospheric region. Below 86 km (i.e. below the high mesosphere), the atmosphere is assumed to be homogeneously mixed with a constant molecular weight. Therefore, the air is treated as a perfect gas and the pressure, density and temperature can be related by the perfect gas law. Above 86 km, the hydrostatic equilibrium progressively breaks down as the contribution of diffusion and vertical transport of the individual species increase. Under these conditions, a dynamically oriented model is required including the diffusive separation. For the experiments discussed here, this treatment can be neglected.

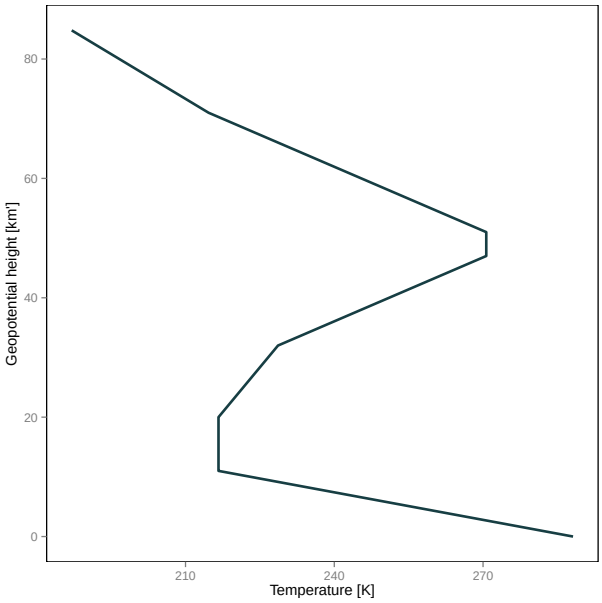

Figure 5.1: ISA-1976 temperature profile derived from NASA (1976).

The set of approximations assumed below 86 km allow to express the dependence between the air temperature, T, and the geopotential height H as a set of linear relationships, often used in standard atmospheres, as

$$T = \alpha(H - H_0) + T_0. \tag{5.2}$$

These linear approaches vary at each thermal layer of the atmosphere (i.e. troposphere, tropopause, stratosphere,...). In Eq. 5.2, H_0 and T_0 are the maximum geopotential height and the temperature in the last atmospheric region, and α defines the lapse rate of the layer (Table 5.1.1 and Fig. 5.1). Surface temperature and pressure are set as 288.15 K and 1013.25 hPa, respectively.

The geopotential height is related with the geometric height z by considering the gravity variation with height as

$$z = \frac{r_t H}{\Gamma r_t - H}. \tag{5.3}$$

Table 5.1: Atmosphere below 86 km (84.8520 kgpm) is divided within 7 regions where the temperature, T, and the geopotential height, Φ, are related by linear relationships. Based on NASA (1976).

Region	α [K/kgpm]	H_0 [kgpm]
Troposphere	-6.5	0
Tropopause	0.0	11
Low Stratosphere	+1.0	20
High Stratosphere	+2.8	32
Stratopause	0.0	47
Low Mesosphere	-2.8	51
High Mesosphere	-2.0	71
		84.8520

Details related to the derivation of Eq. 5.3 can be found in NASA (1976). In this equation r_t is the Earth's radius taken as 6,356,766 m and Γ is 1 gpm m^{-1}.

The use of this correction is not relevant for the experiments presented in this chapter, but it improves the consistency with respect the method proposed for the ISA-1976.

Moreover, the geopotential height in gpm is related with the geopotential ϕ as

$$H = \frac{\phi}{g'}, \tag{5.4}$$

being g' the gravity at surface in units of geopotential taken as 9.80665 gpm s^{-2}.

Finally, pressure p and the geopotential are related through the hypsometric equation derived from the hydrostatic equilibrium. For regions where $\alpha \neq 0$, we have

$$\phi = \frac{T_0}{\alpha}\left(\left(\frac{p_0}{p}\right)^{r_d\alpha/g'} - 1\right). \tag{5.5}$$

Wet atmosphere

For the water vapor, we propose a vertical profile following an exponential relationship between the mixing ratio q_v and the pressure of the kind of

$$q_v(p) = A\exp\Big(-Bp\Big), \tag{5.6}$$

where A and B are two constants. In order to determine these constants, two conditions are required. On the one hand, q_v at surface must be a known value denoted by $q_{v,0}$. On the other hand, at a specific altitude p_2, q_v must be a half of the surface value.

By ordering these conditions to Eq. 5.6, we have

$$A = q_{v,0}\exp\left(-\frac{p_s}{p_2 - p_s}\ln 2\right) \tag{5.7}$$

and

$$B = \frac{\ln 2}{p_2 - p_s}. \tag{5.8}$$

In other words, Eq. 5.6 can be expressed as

$$q_v(p) = q_{v,0} \exp\left(- \frac{p_s - p}{p_s - p_2} \ln 2 \right). \tag{5.9}$$

In spite of the simplification in the water vapor profile, Eq. 5.9 provides a realistic behavior showing a high concentration near to the surface where the sources are found and decreasing quickly with the altitude.

An example of the form of Eq. 5.2 is provided in Fig. 5.2 by assuming standard conditions of pressure and temperature, a p_2 of 925 hPa and RH of 100% at surface.

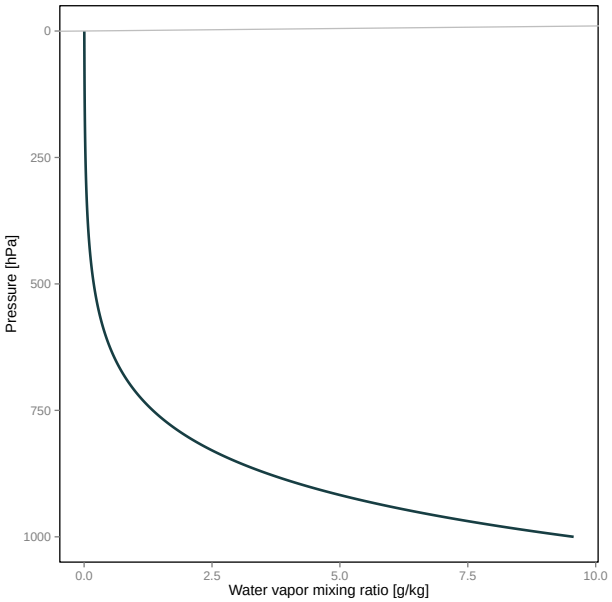

Figure 5.2: Water vapor mixing ratio profile derived from Eq. 5.9 by assuming standard conditions of pressure and temperature, a p_2 of 925 hPa and RH of 100% at surface.

In order to design the experiments, it is easier to work in terms of the relative humidity, RH, rather than the water mixing ratio. The conversion from one to the other is performed following Bolton (1980) as in many parts of the WRF-ARW model. The saturation water vapor pressure, e_s, is defined as

$$e_s = 6.112 \exp\left(\frac{17.67T}{T + 243.5} \right), \tag{5.10}$$

being T expressed in Celsius degree.

By assuming that the specific humidity and the water vapor mixing ratio are equivalent, the water vapor pressure e can be expressed as

$$e = \frac{pq_v}{0.622}, \tag{5.11}$$

Eqs. 5.10 and 5.11 lead to express RH as

$$RH = 100 \frac{q_v}{q_{v,s}} = 100 q_v \frac{(p - e_s)}{0.622 e_s}, \tag{5.12}$$

Cloudy atmosphere

Adding ideal clouds with some degree of realism is not an easy job. As it has been discussed in previous chapters, the information relative to clouds provided by the model is expressed on mixing ratios of hydrometeors, i.e. mass of hydrometeors per mass of dry air. In general, these variables show a high variation cloud by cloud and it is hard to obtain direct measurements about them. Moreover, the related literature is not too large, with the exception of the publications focused on the microphysics schemes and a peak of interest during second half of the last century. Therefore, a set of vertical profiles were created for developing the experiments presented in this chapter in a field that could be an entire thesis.

Furthermore, there are many degrees of freedom to be tested. For example, cloud layers at different heights can be overlapped with different sky fractions, clouds can have different thicknesses, distinct bases and multiple composition.

For this reason some assumptions have been necessary for the development of these experiments. Basically, there are three major approximations: i) clouds are only allowed in contiguous layers, ii) clouds are assumed as stratus that cover the entire grid-point (i.e. overcast) and iii) clouds are only composed by cloud droplets and ice crystals hence, hydrometeors such as rain, snow and graupel are neglected.

In order to create the cloud profiles, let us consider an air particle lifted adiabatically from the surface with a vapor mixing ratio $q_{v,0}$. As the process is adiabatic, the particle conserves the water vapor while temperature decreases with a lapse rate of 1 K per 100 m.

Thereupon, as the particle lifts, the saturation vapor pressure decreases while the relative humidity increases. There is a level in which the particle becomes saturated. This level is called *Lifting Condensation Level* (LCL) and due to the mass conservation, the water vapor at this level is

$$q_{LCL} = q_{v,0}. \tag{5.13}$$

From that level, as the particle rises, the saturation threshold continues decreasing and the water vapor surplus condensates in water droplets or freezes in ice crystals. Under this hypothesis, the lifting process remains adiabatic inside the cloud (i.e. saturated adiabatic) and thus, the water content of the particle must be conserved. As will be discussed below, this hypothesis is not too realistic, but it will be our zero order approach to the problem.

At a level j inside to the cloud, the total water mixing ratio, $q_{s,j}$, will be the sum of the saturated water vapor, $q_{v,sat}(T_j)$, and the adiabatic liquid/ice mixing ratio, $q_{s,ad,j}$, as

$$q_{s,j} = q_{v,sat} + q_{s,ad,j} = q_{LCL} = q_{v,0}. \tag{5.14}$$

As the process is assumed adiabatic, $q_{s,j}$ must be the same that in the LCL and hence, the same that at surface. Furthermore, $q_{v,sat}$ can be obtained from Eq. 5.12 given the temperature and pressure of the layer.

Then, the magnitude of interest for creating the artificial clouds is $q_{s,ad,j}$. As it was detailed in Pruppacher and Klett (2010), formerly $q_{s,ad,j}$ follows complex expressions for liquid and for ice phases that only can be solved by using numerical methods. However, as $q_{s,j}$ and $q_{v,sat}$ are two well known magnitudes, $q_{s,ad,i}$ can be derived from Eq. 5.14 as

$$q_{s,ad,j} = q_{v,0} - q_{v,sat}. \tag{5.15}$$

Generally, real clouds are not adiabatic because the condensed water vapor is transformed to other hydrometeors by exchanging energy with the medium. Moreover, the external drier air is constantly entrained inside the cloud at all levels and it is mixed with the cloud particles, breaking down the adiabatic approach. Warner (1970) showed that the ratio between the real liquid/ice water mixing ratio, $q_{s,real,j}$, decreases with height, being maximum at the cloud base, and increasing with the cloud thickness. Typically, the ratio between $q_{s,real,j}$ and $q_{s,ad,j}$ ranges from 0.1 to 0.6, being around 1 near the cloud base (Blyth and Latham, 1990).

Warner (1955) analyzed the relationship between $q_{s,real,j}$ and $q_{s,ad,i}$. Based on the results presented in that paper, $q_{s,ad,i}$ can be corrected with the following adjustment,

$$\frac{q_{s,real,j}}{q_{s,ad,i}} = -0.155 \ln(z) + 1.471, \tag{5.16}$$

where $z = Z - Z_b$ is the height with respect to the cloud base, Z_b. This curve fits the values proposed by Warner (1955) with a R^2 of 0.9993.

Furthermore, even with the correction introduced by Eq. 5.16, this idealization of the cloud profile shows an important limitation when Z achieves the top of the cloud because the proposed $q_{s,real,j}$ increases monotonically with the height. Notwithstanding, in the real world, the dry particle above the cloud top interacts with the cloud as downdraughts, mixing

vertically with the updraughts (Squires, 1958). Consequently, $q_{s,real,j}$ decreases fast as the cloud layer ends.

Because of the downdraughts depend on many dynamic and thermodynamic factors not considered in these experiments (e.g. wind speed profile), that region is taken into account as a linear decrease in a log-scale in terms the height and avoiding extra approximations. This assumption seems compatible with real measurements observed in Noh et al. (2013) and Warner (1955). Following Noh et al. (2013), the highest LWC value is limited at 0.75 z.

The set of approximations described above are mostly valid for liquid water. Therefore, it is necessary an expression to distinguish liquid cloud droplets $q_{cld,j}$ and $q_{ice,j}$. This distinction is performed by adding a function that depends on temperature called $P(T)$, representing the probability to find the liquid phase.

Based on $P(T)$, $q_{cld,j}$ and $q_{ice,j}$ can be obtained as

$$q_{cld,j} = P(T) q_{s,real,j} \tag{5.17}$$

and

$$q_{ice,j} = (1 - P(T)) q_{s,real,j}. \tag{5.18}$$

The problem now is reduced to find a valid expression for $P(T)$. Following Devasthale and Thomas (2012), $P(T)$ is represented by a quadratic function in terms of two thresholds $T_{min} = 253.15$ K and $T_{max} = 273.15$ K, such as

$$P(T) = \left(\frac{T - T_{min}}{T_{max} - T_{min}} \right)^2. \tag{5.19}$$

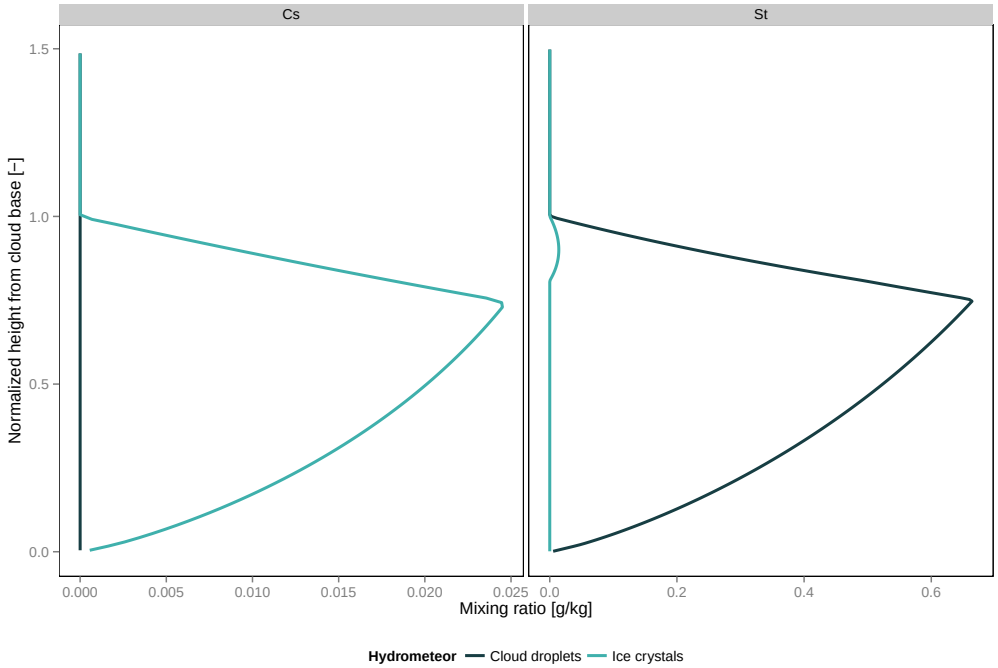

Figure 5.3: Cloud profile for two cases based on the method presented in Sect. 5.1.1. The vertical axis is normalized with respect to the cloud base and top leading to 0 at the base and 1 and at the top. The left-hand plot represents a cloud composed by ice crystals while the right-hand figure shows a cloud composed by cloud droplets with a mixing phase at the top. The settings leading to these profiles are described in Sect. 5.1.2.

In order to reduce the complexity in the determination of the cloud profiles, the calculation is based on two known parameters: the cloud base and top. With these settings, the algorithm evaluates the cloud profile following the next steps:

- **Step 1:** Compute the saturation water mixing ratio at the cloud base. Below the cloud, the water vapor mixing ratio is assumed as a constant with respect to this value (i.e. adiabatic rising, Eq. 5.13).
- **Step 2:** Inside the cloud and below 3/4 of the cloud top, $q_{v,sat}$ is computed at each level following Eq. 5.12.
- **Step 3:** This value is used to calculate $q_{s,ad,j}$ by using Eq. 5.15.
- **Step 4:** As cloud is not adiabatic, $q_{s,ad,j}$ is corrected with Eq. 5.16 leading to $q_{s,real,j}$.
- **Step 5:** Above 3/4 of the cloud top, $q_{s,real,j}$ decreases linearly becoming zero at the top.
- **Step 6:** By using Eqs. 5.17, 5.18 and 5.19, $q_{cld,j}$ and $q_{ice,j}$ are determined at each layer j.
- **Step 7:** Above the cloud top, the water vapor mixing ratio decreases following Eq. 5.9.

An example of the vertical profiles obtained by this method is presented in Fig. 5.3 for two cases: an ice cloud and a water cloud with the presence of ice crystals near the top.

5.1.2 Experiments

The set of ideal vertical profiles described in the previous section can be easily adapted to any vertical configuration providing a high flexibility for designing experiments with different number of vertical levels e_z, distinct vertical distributions of the levels and different TOM values.

Let us imagine an ideal experiment in which a set of vertical levels equidistantly distributed tend to be infinite. In this case, the layer thickness Δz becomes the infinitesimal, dz, and hence, the error due to the assumption that the atmosphere is composed by a finite number of homogeneous layers disappears, i.e. $\epsilon_{trunc} \rightarrow 0$. In the same way, if TOM becomes the TOA, the entire column could be modeled and thus, ϵ_{tom} becomes zero.

In practice, e_z cannot be infinite. However, the first tests with the Sandbox tool revealed an interesting behavior. As the number of vertical levels increase, GHI, DHI and DIF tend to an asymptotic value for all parameterizations. This behavior will be discussed in more detail in the next section but it means that there is a threshold in which all schemes become independent on the number of vertical levels and hence, the truncation error becomes zero.

Furthermore, TOM cannot reach the TOA in these experiments neither. At this point, three issues must be considered. First, the dry atmosphere profile described in the previous section is valid below 86 km (Table 5.1.1). Nevertheless, this is not a real limitation because NASA (1976) includes information above this height. Second, solar parameterizations analyzed in this thesis are designed for NWP models and hence, they do not model the physical processes occurring above 86 km (e.g. ionization). Finally, the upper atmosphere has a very low density and therefore, it has a negligible contribution in the results of the solar schemes.

Therefore, a non-perfect case study can be used as a baseline case in which ϵ_{trunc} and ϵ_{tom} are negligible. This baseline case is defined by a vertical configuration consisting in 2027 vertical levels, equidistantly distributed from 1013.15 hPa to 0.01 hPa (i.e. a layer thickness of around 0.5 hPa).

By using this profile as a baseline, two experiments are performed, one by varying the TOM location and the other by varying the layer thickness. In the first case, ϵ_{trunc} remains as zero

and the results of different TOM settings can be compared with respect to the baseline case. Contrarily, in the second case, ϵ_{tom} is negligible while ϵ_{trunc} can be analyzed.

On the one hand, the study of ϵ_{tom} validates the outcomes of three TOM values: 100, 10 and 1 hPa with respect to the baseline case. These values cover a wide range of the typical settings used in the WRF-ARW model. On the other hand, the analysis of ϵ_{trunc} includes the study of two parameters: i) the number of vertical levels and ii) their vertical distribution. Accordingly, two vertical distributions will be discussed: an equidistant one consisting in a set of η levels uniformly distributed and a logarithmic ideal distribution with a higher density of levels near to the surface and lower density in the upper atmosphere, similar to real applications.

In the logarithmic distribution, each η_k level with $k = 1...e_z$ is defined as

$$\eta_k = \frac{ln(k)}{ln(e_z)}. \tag{5.20}$$

Note that Eq. 5.20 is 0 at surface (k=1) and 1 at the top (k=e_z).

In the case of the TOM error, only a dry atmosphere scenario is tested because at these atmospheric layers water vapor and clouds effects are negligible. The truncation error is analyzed under four scenarios: dry clear-sky atmosphere (DCS), wet clear-sky atmosphere (WCS), water cloud (St) and ice cloud (Cs).

The DCS case is only composed by the dry atmosphere described in Sect. 5.1.1 given by the ISA-1976. In the WCS case, water vapor is included by following Eq. 5.9, assuming a pessimistic situation with a relative humidity of 100% at surface and the parameter p_2 set to 925 hPa. The water vapor mixing profile is presented in Fig. 5.2. Finally, the water cloud (St) and the ice cloud (Cs) are inspired in the stratus and cirrus-stratus. The cloud base is set at 1500 m and 10.000 m, respectively. In both cases, the cloud thickness is defined as 1000 m. These clouds profiles are presented in Fig. 5.3.

In all experiments, a vertical column located in a point defined at 0° latitude and 0° longitude in the 1^{st} of January at 12 UTC, without surface albedo, is considered. The selection of these coordinates is arbitrary since a discussion about the effect due to the latitude or due to the solar zenith angle are not the purposes of this study.

5.2 Results

This section includes the analysis of the results obtained by the set of experiments that were described in Sect. 5.1.2. The analysis of the results is divided in two parts, one dedicated to ϵ_{tom} (Sect. 5.2.1) and the other focused on ϵ_{trun} (Sect. 5.2.2).

This study is focused on the surface irradiance errors as the most representative for solar applications, i.e. GHI, DHI and DIF. In Sect. 5.3, the solar parameterizations will be analyzed from a physical point of view, adding a discussion of the fluxes and the heating rate.

Briefly, the results of the experiments reveal that solar schemes have a significant sensitivity with the number of vertical levels and their distribution, more important in the logarithmic case than in the equidistant one. On the contrary, ϵ_{tom} arises as a residual contribution, less important as the TOM is set at upper levels and for solar parameterizations that use some kind of assumption for the layer between the TOM and the TOA.

The metric used for the following discussion is the relative error defined as the difference between the outcome for the current configuration, f, and the baseline case, b, and normalizing between the last one, i.e.

$$\epsilon_{tom,trun} = \frac{f - b}{b}. \tag{5.21}$$

5.2.1 Analysis of ϵ_{tom}

The analysis of the results by using different TOM values is focused on the DCS scenario because water vapor and clouds does not have a contribution above 100 hPa. The results summarized in Table 5.2 show that the largest errors are produced when TOM is set to 100 hPa and they decrease at 10 and 1 hPa, as expected. The results in this table are presented as relative errors with respect to the baseline case for the same variable.

By variables, the ϵ_{tom} is lower in GHI and DHI than in DIF. The reason of this behavior is explained because GHI and DHI are normalized by a higher value than DIF. In general, DHI is overestimated, while DIF varies from one scheme to each other. As the DHI dominates the GHI under clear sky conditions, the GHI is also overestimated.

Table 5.2: Relative error associated to different TOM settings. The error of each variable is normalized with respect to the baseline value of that variable.

	100 hPa			10 hPa			1 hPa		
[%]	GHI	DHI	DIF	GHI	DHI	DIF	GHI	DHI	DIF
Dudhia	1.1	NA	NA	0.1	NA	NA	0.0	NA	NA
Goddard	0.1	0.1	0.3	0.1	0.1	0.5	0.0	0.0	0.0
New Goddard	0.1	0.1	0.2	0.1	0.1	0.5	0.0	0.0	0.0
RRTMG	0.0	0.0	-0.1	0.0	0.0	-0.1	0.0	0.0	-0.1
CAM	0.9	0.8	5.1	-0.1	-0.1	-0.2	0.0	0.0	0.0
FLG	1.5	2.0	-6.9	0.2	0.2	-0.6	0.0	0.0	-0.1

For a TOM at 100 hPa, the GHI ranges from 0.0% to 1.5%, DHI from near-zero to 2.0% and DIF from -6.9% to 5.1%. These values are strongly reduced when TOM is set at 10 hPa. In this case, the GHI and DHI drift from a slightly negative error of -0.1% to slightly positive with 0.2%. By contrast, DIF varies from -0.6% to 0.5%. Finally, when TOM is set to 1 hPa, errors for GHI and DHI become negligible, while DIF ranges between -0.1% and 0.1%.

RRTMG is the scheme that shows the best results for any TOM with a negligible ϵ_{tom} for GHI and DHI and slightly negative for DIF with -0.1%.

Goddard and New Goddard experience similar results in all tests. When TOM is set at 100 hPa, both schemes show an ϵ_{tom} of 0.1% for GHI and DHI. On the contrary, Goddard shows a higher error for the DIF than New Goddard with 0.3% and 0.2%, respectively. The results are practically the same when TOM is set at 10 hPa with a small increment of the DIF reaching a peak of 0.5%. For a TOM at 1 hPa, ϵ_{tom} becomes negligible.

CAM is an intermediate case. For the highest TOM value, this parameterization experiences a high overestimation of the GHI, DHI and DIF with 0.9%, 0.8% and 5.1%, respectively. For a TOM at 10 hPa, ϵ_{tom} for the three variables drifts from positive values to slightly negative errors with -0.1% for GHI and the DHI, and -0.2% for DIF. When TOM is set to 1 hPa, the error becomes negligible. In contrast to Goddard and New Goddard, CAM also includes an extra layer too but ozone is a constant with respect to the TOM. Thus, when TOM is set at 100 hPa, the layer between the TOM and the TOA is practically considered without ozone, increasing the differences with respect to the baseline case while, when TOM is set at 10 or 1 hPa, the ozone mixing ratio in the layer between the TOM and the TOA is more important, decreasing the error.

In Dudhia, the GHI is overestimated for a TOM set to 100 hPa with a 1.1%. When TOM is lower or equal than 10 hPa, differences with respect to the baseline case become negligible

because the dry air density is very low producing a low contribution in the s_{cs} term of Eq. 3.9. These differences could be higher if Dudhia would consider an ozone profile as will be discussed in the case of FLG. As ozone is not included, this limitation is considered as a contribution into ϵ_{phys} but not in ϵ_{tom}.

Finally, FLG experiences the largest ϵ_{tom} when TOM is set below 10 hPa. For a TOM at 100 hPa, GHI and DHI are strongly overestimated with 1.5% and 2.0% , while DIF shows the worst values with -6.9%. When TOM is set at 10 hPa, the error decreases reaching a 0.2% for GHI and DHI and -0.6% for DIF. At 1 hPa, ϵ_{tom} becomes negligible.

These bad results in FLG are explained for two reasons. On the one hand, the layer between the TOM and the TOA is assumed as transparent, such as in Dudhia. But in contrast to that scheme, FLG considers the absorption due to ozone. Consequently, for a TOM at 100 hPa, the GHI and DHI are strongly overestimated because the ozone peak is missing. As the TOM is set to higher levels, the ozone profile is better represented and hence, the ϵ_{tom} decreases.

5.2.2 Analysis of ϵ_{trunc}

The variation of the vertical levels and their distribution have a significant impact on results of the solar parameterizations. This effect is different from one scheme to each other. Hence, Dudhia and FLG are the most sensitive to the vertical settings while Goddard, New Goddard and CAM produce more constant outcomes. RRTMG is an intermediate case in which for low vertical levels, the variations are important but it reaches a constant value really fast.

Figs. 5.4, 5.5, 5.6 and 5.7 show that as the number of vertical levels increase, irradiances produced by solar schemes tend to achieve an asymptotic value in all scenarios. This value is clearer in the equidistant distribution than in the logarithmic one because the first case uses an uniform resolution, while the logarithmic one improves faster the vertical resolution near to the surface than in the upper levels. Therefore, under the same number of vertical levels, the equidistant distribution has a better representation of the vertical profile than in the logarithmic one.

Schemes under the equidistant distribution reach the asymptotic value around 200 levels (i.e. a thickness of $\sim$5 hPa) in DCS and WCS scenarios (Fig. 5.4) and around 400 levels (i.e. a thickness of $\sim$2.5 hPa) in the cloudy cases, Cs and St (Fig. 5.6).

The convergence in the logarithmic distribution is slower and even some schemes such as Dudhia and FLG cannot reach this value. All schemes are less sensitive under DCS and WCS scenarios (Fig. 5.5) than in the cloudy ones (Fig. 5.7) because cloud properties vary quickly from one vertical configuration to the other.

In conclusion, the assumption of a baseline case composed by 2027 vertical levels equidistantly distributed (i.e. a layer thickness of 0.5 hPa) with a TOM set at 0.01 hPa is appropriated for discussing the truncation and TOM errors. Moreover, differences in the asymptotic value between solar schemes is linked to the distinct approximations used for evaluating the irradiances, described in Chapter 3 and related with ϵ_{phys}. These differences will be analyzed from a physical point of view in the next section.

In the cloudless scenarios (Figs. 5.4 and 5.5), Dudhia is the most sensitive parameterization, overall under 100 vertical levels in the equidistant distribution while in the logarithmic one, this scheme shows a high variation for any number of levels.

The other schemes experience distinct behaviors for GHI, DHI and DIF. The lowest dependence on the vertical configuration is observed in GHI being RRTMG and FLG, the codes with the highest variations. Conversely, DHI and DIF show significant variations below 100 levels.

As the number of vertical levels decrease, all schemes tend to model a more transparent atmosphere (i.e. higher DHI), with the exception of FLG that experience a reverse pattern leading to a more opaque atmosphere. Regarding the scattering represented by DIF, RRTMG shows a less scattering atmosphere as the number of vertical levels decrease while the other schemes show the opposite behavior.

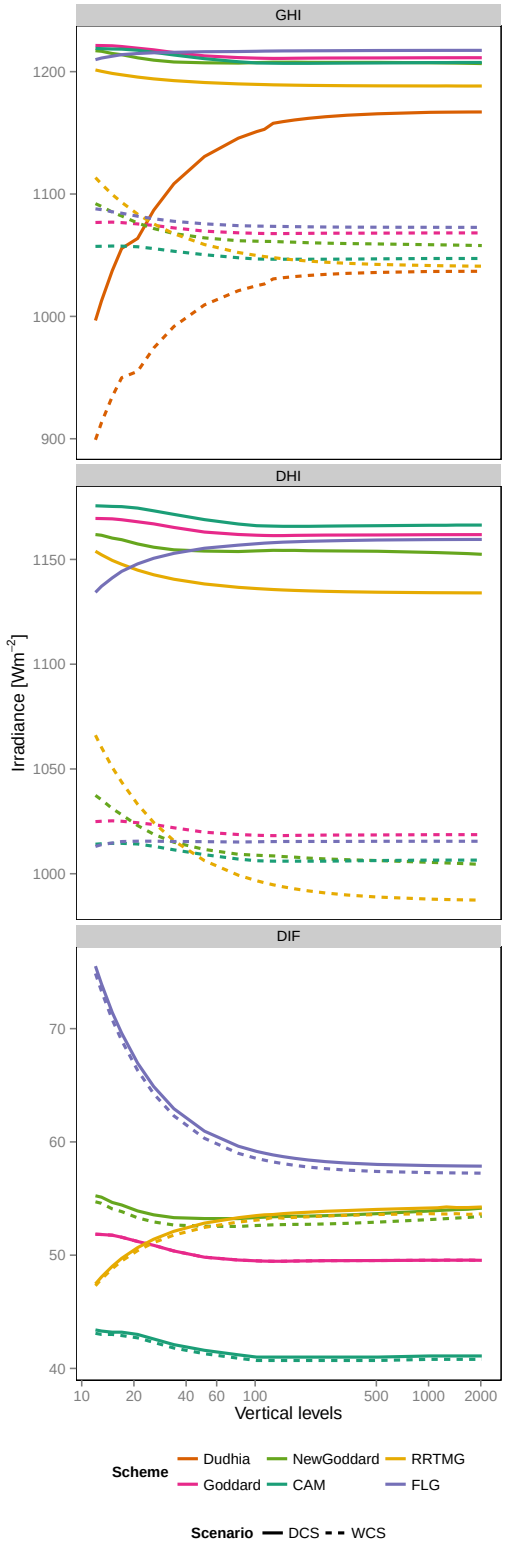

Figure 5.4: Variation of the surface irradiances in terms of the number of vertical levels equidistantly distributed. The solid lines correspond to the DCS scenario while the dashed lines are the WCS.

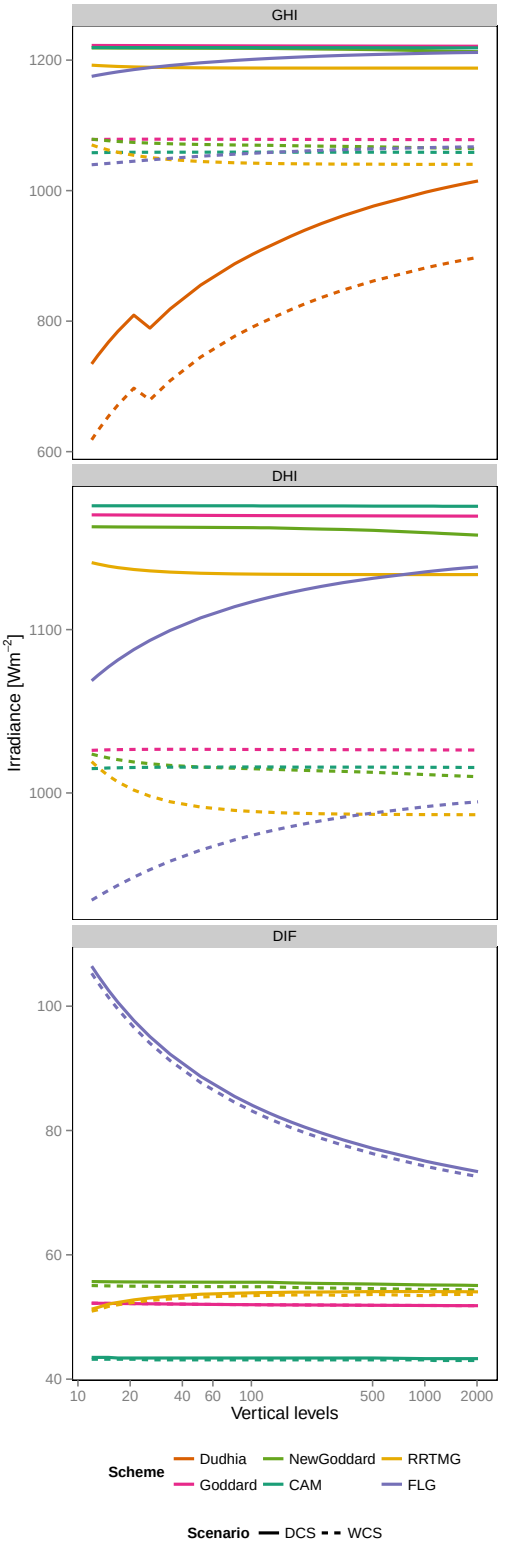

Figure 5.5: Variation of the surface irradiances in terms of the number of vertical levels logarithmically distributed. The solid lines correspond to the DCS scenario while the dashed lines are the WCS.

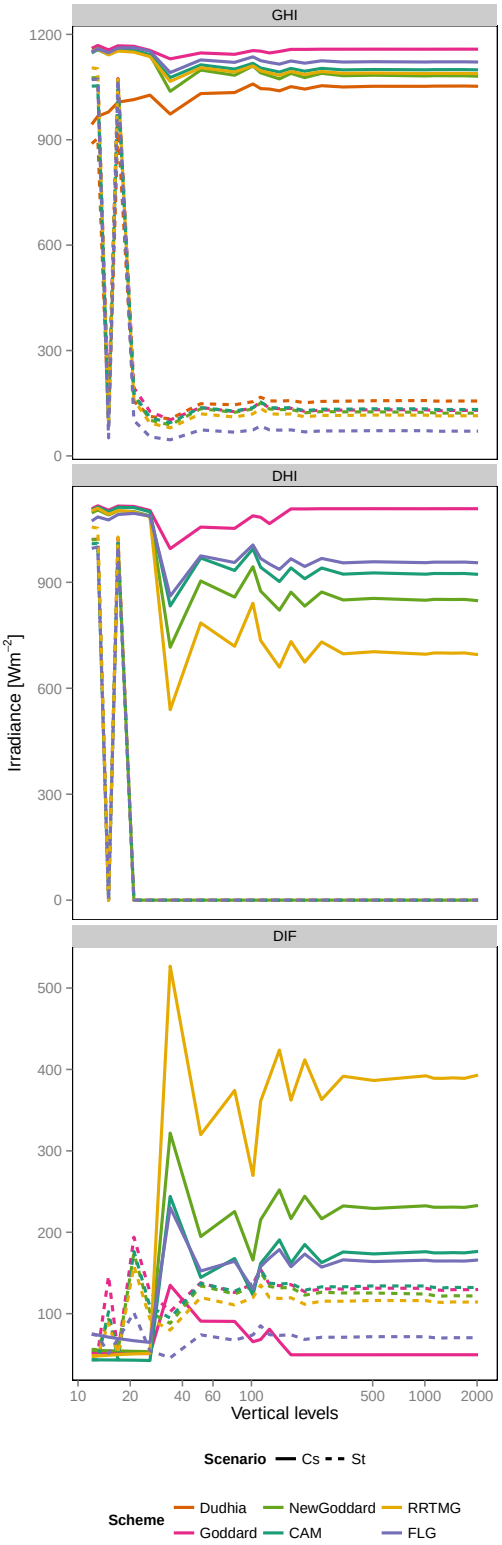

Figure 5.6: Variation of the surface irradiances in terms of the number of vertical levels equidistantly distributed. The solid lines correspond to the CLD-Cs scenario while the dashed lines are the CLD-St.

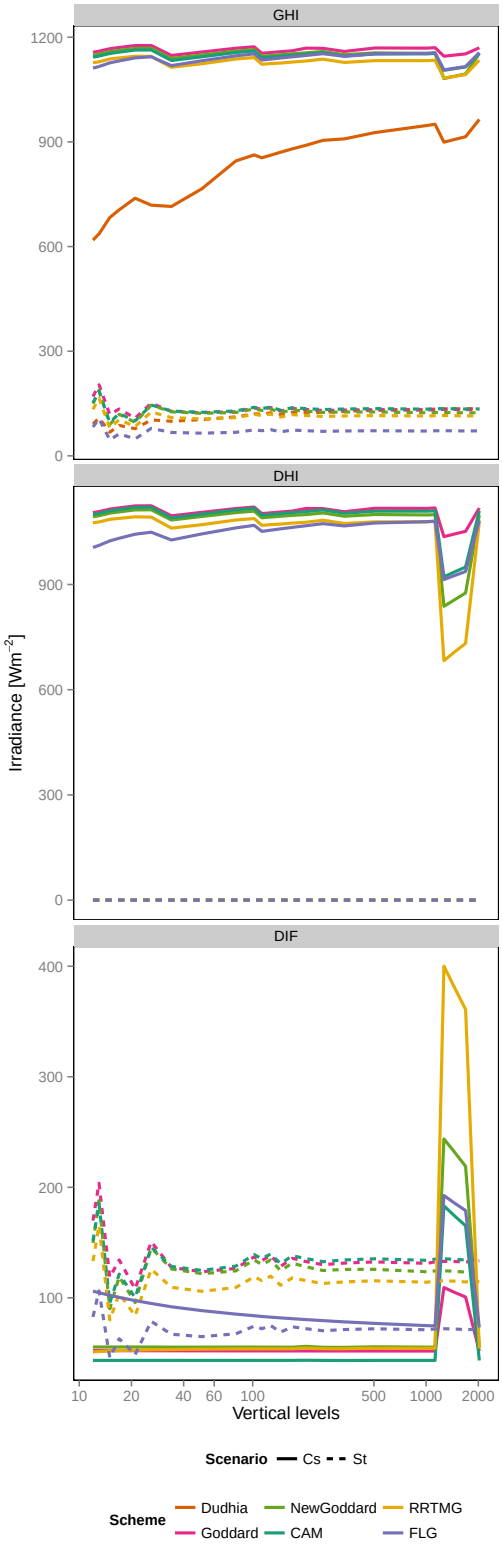

Figure 5.7: Variation of the surface irradiances in terms of the number of vertical levels logarithmically distributed. The solid lines correspond to the CLD-Cs scenario while the dashed lines are the CLD-St.

Furthermore, these differences are masked in cloudy scenarios (Figs. 5.4 and 5.5) because the properties of the cloudy layers have a more important role.

In order to quantify ϵ_{trun}, Tables 5.3, 5.4, 5.5 and 5.5 are presented. These tables show the relative error of GHI, DHI and DIF for the range of vertical levels widely used in mesoscale applications, i.e. from 30 to 80 with intervals of 10.

As shown in the previous figures, ϵ_{trun} tends to decrease with the number of vertical levels and it is larger in the logarithmic distribution than in the equidistant one. By scenarios, the lowest truncation error is produced in the DCS case and it increases as more physical elements are introduced.

Cloudless sky conditions: DCS and WCS scenarios

Under cloudless sky conditions (Tables 5.3 and 5.4), Dudhia is the scheme with the worst results. In both scenarios, the GHI is highly underestimated or, in other words, Dudhia produces a too opaque atmosphere as the number of vertical levels decrease. In the DCS scenario, ϵ_{trun} ranges from -5.8% to -1.8% under the equidistant distribution and from -31.0% to -23.9% under the logarithmic one. In the WCS case, the truncation error fluctuates from -5.1% to -1.5% and from -32.9% to -25.1%, respectively.

In Goddard, the three irradiances tend to be overestimated. In the case of the equidistant distribution, ϵ_{trun} in GHI and DHI drift from 0.4% to near-zero, while in DIF varies from 2.1% to 0.1%. Furthermore, ϵ_{trun} in the logarithmic case experiences small variations in the range from 30 to 80 vertical levels. GHI and DHI are practically constant with 0.9% and 0.7%, respectively, whereas DIF ranges from 5.2% to 4.9%. The addition of water vapor has a small impact on ϵ_{trun} for both vertical distributions as it can be observed in Table 5.4.

New Goddard experiences a more complex behavior. In the equidistant case, GHI and DHI are slightly overestimated while DIF is underestimated. In the DCS scenario, ϵ_{trun} in GHI drifts from 0.2% to near-zero. The DHI shows small variations around 0.1% and 0.2% for any number of vertical levels. Finally, in DIF, ϵ_{trun} ranges between -1.4% and -1.7%. In the WCS case, ϵ_{trun} becomes more relevant. In GHI and DHI, it varies from 1.2% to 0.4%, while in DIF from -1.3% to -1.7%.

The logarithmic distribution shows a clear overestimation of the three variables. In the DCS case, this scheme shows the same results for all the vertical configurations from 30 to 80 vertical levels with and error of 1.0%, 0.9% and 2.7% in GHI, DHI and DIF, respectively. In the WCS, ϵ_{trun} experiences a small variation with the number of vertical levels. GHI ranges from 1.4% to 1.1%, DHI from 1.3% to 1.1% and DIF from 2.8% to 2.7%.

RRTMG overestimates GHI and DHI and underestimates the DIF whatever the number of vertical levels. In the dry atmosphere scenario (Table 5.3), ϵ_{trun} in GHI varies from 0.4% to 0.1%, DHI from 0.7% to 0.2% and DIF from -4.5% to -1.7%, in the equidistant case. Conversely, in the logarithmic distribution, GHI and DHI experience near-zero errors, while DIF ranges between -1.8% to -0.8%.

The truncation error under the wet atmosphere scenario increases considerably (Table 5.4). In the equidistant distribution, ϵ_{trun} varies from 2.9% to 1.1%, from 3.3% to 1.2% and from -4.0% to -1.3%, in GHI, DHI and DIF, respectively. The error in the logarithmic distribution is lower with a variation between 0.8% and 0.2%, 0.9% and 0.2% and from -1.5% to -0.5%, in GHI, DHI and DIF.

CAM shows a similar behavior that described for Goddard, in the DCS scenario as in WCS case. For all the configurations, the irradiances are overestimated, decreasing with the number of vertical levels. In the DCS scenario, the error in GHI and DHI varies from 0.6% to near-zero in the equidistant case, while it remains between 1% and 0.8% in the logarithmic distribution. The truncation error in DIF ranges from 2.9% to 0.2% in the equidistant distribution and it remains around 5.6% in the second distribution.

In the wet atmosphere, ϵ_{trun} varies overall for GHI and DHI. In the equidistant distribution, ϵ_{trun} drifts from 0.7% to 0.1% in GHI and from 0.6% to near-zero in DHI. For the logarithmic case, errors increase similarly. In GHI and DHI, ϵ_{trun} is around 1.1% and 0.9%, respectively, for all the configurations.

Finally, FLG produces a different pattern that the observed in the other schemes. GHI and DHI tend to be underestimated while DIF tends to be overestimated producing the largest errors for this variable with respect to the other schemes. For the equidistant distribution in the dry atmosphere scenario, GHI varies slowly with a near-zero ϵ_{trun}. DHI varies from -0.7% to 0.2%, while DIF ranges from 10.2% to 3.0%. In the logarithmic configuration, the error increase considerably. GHI decreases from -2.2% to -1.5%, DHI from -5.4% to -3.9% and, finally, DIF from 61.6% to 47.7%.

With water vapor, ϵ_{trun} increase as in the previous schemes. In the equidistant case, GHI and DHI drift from near-zero values to positive errors, in the first field ranging from 0.5% to 0.1% and, being near-zero in the second variable. DIF shows a low variation, with errors decreasing from 10.3% to 3.1%. In the logarithmic distribution, ϵ_{trun} maintains the same pattern discussed for the DCS scenario. GHI varies from -2.3% to -1.6%, DHI from -5.9% to -4.4%, and DIF from 61.6% to 47.7%.

Cloudy sky conditions: St and Cs scenarios

Under the cloudy sky conditions, the observed patterns become more complex. In the case of the low cloud layer configuration shown in Table 5.5, ϵ_{trun} is better in the logarithmic case that in the equidistant one. In the first distribution, the lower layers has a better vertical resolution, this configuration lead to a better description of the cloud features faster than the equidistant case. Dudhia is an exception producing better results in the second distribution than in the first one.

Under this cloud scenario, DHI becomes zero and, trivially, errors in GHI and DIF are the same. In the equidistant case, ϵ_{trun} varies between -10.7% and -6.9% in Dudhia, -2.9% and 13.5% in Goddard, -3.2% and 10.4% in New Goddard, -3.2% and 6.9% in RRTMG, -7.7% and 5.4% in CAM and between -9.5% and 5.6% in FLG. Conversely, in the logarithmic distribution, ϵ_{trun} drifts from -34.6% to -28.5% in Dudhia, from 8.9% to -2.5% in Goddard, from 2.2% to 17.9% in New Goddard, from -4.1% to 9.1% in RRTMG, from -2.9% to 9.8% in CAM and from -4.7% to 11.2% in FLG.

By contrast, the case with the high cloud layer has more degrees of freedom. In general, the equidistant distribution experiences better results than the logarithmic case because the upper layers are better represented in the first distribution than in the second one. Moreover, ϵ_{trun} varies irregularly with the number of vertical levels because the cloud properties change quickly from one configuration to each other. Nevertheless, the main tendency is to reduce ϵ_{trun} with the number of vertical levels due to the logarithmic behavior of the pressure profile.

In the equidistant distribution, Dudhia experiences the lower ϵ_{trun}. In general, all the configurations underestimate the GHI, with the exception of the case with 40 vertical levels in which ϵ_{trun} is 1.0%. The truncation error is maximum with -2.5% when e_z is set to 50 and 70 vertical levels and with a minimum of -0.3% when the experiment is set with 60 vertical levels.

The case of Goddard is misleading. As it can be observed in Table 5.5 errors for this parameterization are very low and similar to the WCS case. As it was described in Sect. 3.4, this scheme has a high threshold for considering clouds. This threshold was relaxed in New Goddard allowing clouds with lower optical thicknesses. The cloud properties used in this experiment are not enough for Goddard and hence, this scheme considers a clear sky scenario. This issue will discussed in more detail in Sect.5.3.

The other schemes start with a high overestimation and underestimation of the DHI and DIF, respectively, that leads to a low overestimation in GHI. In the equidistant distribution,

ϵ_{trun} in New Goddard drifts from 5.7% to 0.3% in GHI, from 28.4% to 1.2% in DHI and from -77.2% to -3.2% in DIF. In RRTMG, the errors drifts from 4.5% to 0.4%, from 56.1% to 3.4% and from -86.8% to -4.8%, respectively. In CAM from 3.9% to 0.2%, from 19.2% to 1.2% and from -76.1% to -4.9%. Finally, ϵ_{trun} in FLG decreases from 2.9% to -0.1 in GHI, from 14.1% to 0.1 in DHI and from -61.7% to -0.9%, respectively.

For a low number of vertical levels (i.e. less than 50), the logarithmic distribution produce similar results than the equidistant case. On the contrary, for configurations with a larger number of vertical levels, ϵ_{trun} does not decrease as in the equidistant case. In a configuration consisting in 80 vertical levels, New Goddard shows an error of 7.4%, 30.3% and -76.2% in GHI, DHI and DIF, respectively. In RRTMG, ϵ_{trun} becomes 4.5%, 55.9% and -86.3% and in CAM of 5.2%, 20.6% and -75.4%, for the same variables and the same configuration.

Dudhia and FLG are two exceptions in this description. In the first scheme, the error decreases strongly with the number of vertical levels, from -33.8% to -19.6%. In the second parameterization, ϵ_{trun} has the same behavior that in the previous schemes but it is significantly lower. For a configuration consisting in 80 vertical levels, the truncation error in GHI is 2.3%, in DHI 11.1% and in DIF -48.6%.

5.3 Physical discussion

Besides the discussion of the truncation and TOM errors, the set of experiments presented in this chapter provide valuable information regarding the physical impact of the different approximations assumed by each parameterization. In this section, the differences between solar schemes will be discussed analyzing the outcomes for the baseline case because it does not have the contribution of the truncation and the TOM error. First, the surface irradiances are discussed in Sect. 5.3.1 and then, the behavior of the shortwave fluxes and the heating rate profile at each layer, in Sect. 5.3.2.

5.3.1 Physical discussion of the asymptotic irradiances

The DCS scenario provides information about the molecular processes. As it was described in Sects. 2.5.1 and 2.5.2, the physical processes that contribute to the beam attenuation and scattering in a dry clear-sky atmosphere are the molecular absorption and the Rayleigh scattering. Differences in the parameterization of the radiative variables and in the treatment of the spectral integration lead to different asymptotic values for each scheme (Table 5.7).

With the exception of Dudhia and RRTMG, all schemes show similar results for the GHI. Goddard, New Goddard and CAM produce similar results with 1211, 1207 and 1208 Wm^{-2}, respectively. FLG reaches the highest GHI with 1217 Wm^{-2}, very close to the previous ones. RRTMG produces the lowest GHI of all schemes that solve the RTE with 1188 Wm^{-2}. Finally, the default version of Dudhia (i.e. with swrad_scat=1) shows the lowest GHI with 1167 Wm^{-2}. As detailed in Sect. 3.3, the parameter swrad_scat is the only element that reduces the solar beam in a dry atmosphere. Therefore, by modifying this factor, Dudhia can experience a more transparent or a more opaque atmosphere depending on the user's specifications.

The study of the DHI shows similar results. The RRTMG experiences the most opaque atmosphere with 1134 Wm^{-2}. The other parameterizations produce similar DHI results, being CAM the case with the most transparent atmosphere, 1166 Wm^{-2}, very similar to Goddard, FLG and New Goddard with 1162, 1160 and 1152 Wm^{-2}, respectively. As aerosols are disabled in these experiments (Sect. 5.1), the elements that contribute to the attenuation of the direct beam are the atmospheric gasses, mostly ozone, oxygen and carbon dioxide.

RRTMG has many elements to become the parameterization that models the most opaque atmosphere under dry atmosphere conditions as it is described by Fig. 3.3. First, this scheme considers a large number of gas species that contribute to the absorption with a high spectral

Table 5.3: Results of the truncation error for the most common number of vertical levels used in mesoscale simulations under the DCS scenario. The error of each variable is normalized with respect to the baseline case for the same field. The first part of the table corresponds to the equidistant distribution while the second part shows the results for the logarithmic case. DHI and DIF for Dudhia are not defined because this scheme does not solve explicitly the RTE.

		30			40			50			60			70			80		
	[%]	GHI	DHI	DIF	GHI	DHI	DIF	GHI	DHI	DIF	GHI	DHI	DIF	GHI	DHI	DIF	GHI	DHI	DIF
Equidistant	Dudhia	-5.8	NA	NA	-4.2	NA	NA	-3.2	NA	NA	-2.6	NA	NA	-2.1	NA	NA	-1.8	NA	NA
	Goddard	0.4	0.4	2.1	0.2	0.2	1.1	0.1	0.1	0.6	0.1	0.1	0.3	0.0	0.0	0.2	0.0	0.0	0.1
	New Goddard	0.2	0.2	-1.4	0.1	0.2	-1.6	0.1	0.1	-1.7	0.0	0.1	-1.7	0.0	0.1	-1.7	0.0	0.1	-1.7
	RRTMG	0.4	0.7	-4.5	0.3	0.5	-3.3	0.2	0.4	-2.7	0.2	0.3	-2.2	0.2	0.3	-1.9	0.1	0.2	-1.7
	CAM	0.6	0.5	2.9	0.4	0.3	1.9	0.3	0.2	1.2	0.2	0.1	0.7	0.1	0.1	0.2	0.0	0.0	0.2
	FLG	-0.1	-0.7	10.2	-0.1	-0.5	7.2	-0.1	-0.4	5.5	-0.1	-0.3	4.4	-0.1	-0.3	3.6	-0.1	-0.2	3.0
Logarithmic	Dudhia	-31.0	NA	NA	-28.5	NA	NA	-26.9	NA	NA	-25.6	NA	NA	-24.7	NA	NA	-23.9	NA	NA
	Goddard	0.9	0.7	5.2	0.9	0.7	5.1	0.9	0.7	5.0	0.9	0.7	5.0	0.9	0.7	5.0	0.9	0.7	4.9
	New Goddard	1.0	0.9	2.7	1.0	0.9	2.7	1.0	0.9	2.7	1.0	0.9	2.7	1.0	0.9	2.7	1.0	0.9	2.7
	RRTMG	0.0	0.1	-1.8	0.0	0.1	-1.4	-0.0	0.0	-1.1	-0.0	0.0	-1.0	-0.0	0.0	-0.8	-0.0	0.0	-0.8
	CAM	1.0	0.8	5.6	1.0	0.8	5.6	1.0	0.8	5.6	1.0	0.8	5.6	1.0	0.8	5.6	1.0	0.8	5.6
	FLG	-2.2	-5.4	61.6	-2.0	-4.9	56.8	-1.8	-4.5	53.6	-1.7	-4.3	51.2	-1.6	-4.1	49.3	-1.5	-3.9	47.7

Table 5.4: Results of the truncation error for the most common number of vertical levels used in mesoscale simulations under the WCS scenario. The error of each variable is normalized with respect to the baseline case for the same field. The first part of the table corresponds to the equidistant distribution while the second part shows the results for the logarithmic case. DHI and DIF for Dudhia are not defined because this scheme does not solve explicitly the RTE.

		30			40			50			60			70			80		
	[%]	GHI	DHI	DIF	GHI	DHI	DIF	GHI	DHI	DIF	GHI	DHI	DIF	GHI	DHI	DIF	GHI	DHI	DIF
Equidistant	Dudhia	-5.1	NA	NA	-3.6	NA	NA	-2.7	NA	NA	-2.2	NA	NA	-1.8	NA	NA	-1.5	NA	NA
	Goddard	0.5	0.4	2.1	0.3	0.2	1.2	0.1	0.1	0.6	0.1	0.1	0.3	0.0	0.0	0.2	0.0	0.0	0.1
	New Goddard	1.1	1.2	-1.3	0.8	0.9	-1.5	0.6	0.7	-1.6	0.5	0.6	-1.7	0.4	0.5	-1.7	0.4	0.5	-1.7
	RRTMG	2.9	3.3	-4.0	2.2	2.4	-2.9	1.7	1.9	-2.3	1.4	1.6	-1.8	1.2	1.4	-1.6	1.1	1.2	-1.3
	CAM	0.7	0.6	2.9	0.4	0.4	2.0	0.3	0.3	1.2	0.2	0.2	0.7	0.1	0.1	0.5	0.1	0.0	0.2
	FLG	0.5	0.0	10.3	0.4	-0.0	7.2	0.3	-0.0	5.5	0.2	-0.0	4.4	0.2	-0.0	3.6	0.1	-0.0	3.1
Logarithmic	Dudhia	-32.9	NA	NA	-30.1	NA	NA	-28.3	NA	NA	-27.0	NA	NA	-25.9	NA	NA	-25.1	NA	NA
	Goddard	1.0	0.8	5.2	1.0	0.8	5.1	1.0	0.8	5.0	1.0	0.8	5.0	1.0	0.8	5.0	1.0	0.8	4.9
	New Goddard	1.4	1.3	2.8	1.3	1.2	2.7	1.2	1.1	2.7	1.2	1.1	2.7	1.2	1.1	2.7	1.1	1.1	2.7
	RRTMG	0.8	0.9	-1.5	0.5	0.6	-1.1	0.4	0.4	-0.8	0.3	0.3	-0.7	0.2	0.2	-0.5	0.2	0.2	-0.5
	CAM	1.1	0.9	5.6	1.1	0.9	5.6	1.1	0.9	5.6	1.1	0.9	5.6	1.1	0.9	5.6	1.1	0.9	5.6
	FLG	-2.3	-5.9	61.6	-2.0	-5.4	56.8	-1.9	-5.0	53.5	-1.8	-4.7	51.1	-1.7	-4.5	49.2	-1.6	-4.4	47.7

Table 5.5: Results of the truncation error for the most common number of vertical levels used in mesoscale simulations under the St scenario. The error of each variable is normalized with respect to the baseline case for the same field. The first part of the table corresponds to the equidistant distribution while the second part shows the results for the logarithmic case. DHI and DIF for Dudhia are not defined because this scheme does not solve explicitly the RTE. In this scenario, the cloud layer attenuates all the direct beam and thus, the error is not defined for the other schemes.

		30			40			50			60			70			80		
	[%]	GHI	DHI	DIF	GHI	DHI	DIF	GHI	DHI	DIF	GHI	DHI	DIF	GHI	DHI	DIF	GHI	DHI	DIF
Equidistant	Dudhia	-10.7	NA	NA	-14.5	NA	NA	-6.2	NA	NA	-3.4	NA	NA	-8.3	NA	NA	-6.9	NA	NA
	Goddard	13.5	NA	13.5	-2.2	NA	-2.2	4.9	NA	4.9	5.8	NA	5.8	-4.4	NA	-4.4	-2.9	NA	-2.9
	New Goddard	10.4	NA	10.4	-3.2	NA	-3.2	8.6	NA	8.6	11.5	NA	11.5	0.6	NA	0.6	1.9	NA	1.9
	RRTMG	6.9	NA	6.9	-7.8	NA	-7.8	3.4	NA	3.4	6.0	NA	6.0	-4.6	NA	-4.6	-3.2	NA	-3.2
	CAM	5.4	NA	5.4	-7.7	NA	-7.7	2.5	NA	2.5	5.0	NA	5.0	-4.7	NA	-4.7	-3.4	NA	-3.4
	FLG	5.6	NA	5.6	-9.5	NA	-9.5	3.0	NA	3.0	6.0	NA	6.0	-5.8	NA	-5.8	-4.3	NA	-4.3
Logarithmic	Dudhia	-34.6	NA	NA	-34.6	NA	NA	-26.4	NA	NA	-26.5	NA	NA	-27.8	NA	NA	-28.5	NA	NA
	Goddard	8.9	NA	8.9	-2.5	NA	-2.5	12.0	NA	12.0	8.7	NA	8.7	1.6	NA	1.6	-2.4	NA	-2.4
	New Goddard	12.7	NA	12.7	3.4	NA	3.4	17.9	NA	17.9	13.4	NA	13.4	6.3	NA	6.3	2.2	NA	2.2
	RRTMG	4.2	NA	4.2	-4.4	NA	-4.4	9.1	NA	9.1	5.6	NA	5.6	-0.7	NA	-0.7	-4.3	NA	-4.3
	CAM	4.9	NA	4.9	-2.9	NA	-2.9	9.8	NA	9.8	6.5	NA	6.5	0.7	NA	0.7	-2.6	NA	-2.6
	FLG	4.8	NA	4.8	-4.7	NA	-4.7	11.2	NA	11.2	6.9	NA	6.9	-0.1	NA	-0.1	-4.3	NA	-4.3

Table 5.6: Results of the truncation error for the most common number of vertical levels used in mesoscale simulations under the Cs scenario. The error of each variable is normalized with respect to the baseline case for the same field. The first part of the table corresponds to the equidistant distribution while the second part shows the results for the logarithmic case. DHI and DIF for Dudhia are not defined because this scheme does not solve explicitly the RTE.

		30			40			50			60			70			80		
	[%]	GHI	DHI	DIF	GHI	DHI	DIF	GHI	DHI	DIF	GHI	DHI	DIF	GHI	DHI	DIF	GHI	DHI	DIF
Equidistant	Dudhia	-1.2	NA	NA	1.0	NA	NA	-2.5	NA	NA	-0.3	NA	NA	-2.5	NA	NA	-1.7	NA	NA
	Goddard	-0.3	-0.4	2.1	0.4	0.4	1.2	-1.2	-5.3	90.5	0.3	0.3	0.3	-1.3	-5.6	96.0	-1.3	-5.0	82.7
	New Goddard	5.7	28.4	-77.2	6.2	29.0	-77.0	1.1	4.5	-11.5	3.0	12.6	-31.9	-0.6	-2.7	7.4	0.3	1.2	-3.2
	RRTMG	4.5	56.1	-86.8	4.8	56.4	-86.6	1.1	9.8	-14.1	2.5	23.6	-34.9	-0.1	-4.1	7.0	0.4	3.4	-4.8
	CAM	3.9	19.2	-76.1	4.3	19.7	-76.3	0.9	3.7	-13.8	2.1	8.9	-33.3	-0.3	-1.7	7.3	0.2	1.2	-4.9
	FLG	2.9	14.1	-61.7	3.5	15.0	-62.7	0.2	1.0	-4.6	1.4	5.4	-21.3	-0.5	-2.2	9.0	-0.1	0.1	-0.9
Logarithmic	Dudhia	-33.8	NA	NA	-30.0	NA	NA	-27.4	NA	NA	-25.5	NA	NA	-20.6	NA	NA	-19.6	NA	NA
	Goddard	-1.1	-1.4	5.2	-0.5	-0.8	5.1	-0.0	-0.3	5.0	0.3	0.1	5.0	0.7	0.5	5.0	0.9	0.7	4.9
	New Goddard	5.1	27.4	-76.2	5.8	28.3	-76.2	6.3	29.0	-76.2	6.7	29.4	-76.2	7.1	30.0	-76.2	7.4	30.3	-76.2
	RRTMG	2.0	52.1	-86.5	2.7	53.2	-86.4	3.3	53.9	-86.4	3.6	54.5	-86.4	4.3	55.6	-86.3	4.5	55.9	-86.3
	CAM	2.8	17.8	-75.4	3.5	18.6	-75.4	4.0	19.3	-75.4	4.4	19.7	-75.4	4.9	20.3	-75.4	5.2	20.6	-75.4
	FLG	-0.7	6.9	-43.9	0.3	8.3	-45.5	1.0	9.2	-46.6	1.5	9.9	-47.5	2.0	10.6	-48.1	2.3	11.1	-48.6

Table 5.7: Results of the different schemes for the baseline case consisting in 2027 vertical levels equidistantly distributed (i.e. a layer thickness of 0.5 hPa) and a TOM set to 0.01 hPa.

[Wm^{-2}]	Dudhia			Goddard			New Goddard			CAM			RRTMG			FLG		
Scenario	GHI	DHI	DIF	GHI	DHI	DIF	GHI	DHI	DIF	GHI	DHI	DIF	GHI	DHI	DIF	GHI	DHI	DIF
DCS	1167	NA	NA	1211	1160	51	1207	1152	55	1208	1166	42	1188	1134	54	1217	1162	55
WCS	1037	NA	NA	1068	1068	49	1058	1004	44	1047	1007	40	1041	987	54	1073	1016	57
St	156	NA	NA	130	0	130	122	0	122	130	0	130	114	0	114	71	0	71
Cs	1052	NA	NA	1157	1105	52	1081	848	233	1088	923	165	1099	695	404	1121	935	186

resolution provided by the CKD method (Sect. 3.6). Second, because this scheme uses the highest CO_2 concentration with 376 ppmv. Finally, the ozone profile used by RRTMG reaches a high peak in the stratosphere (Fig. 3.6).

Conversely, CAM models the most transparent atmosphere because this scheme is full transparent in the PAR spectral region and ozone, carbon dioxide and oxygen absorb in small spectral regions compared with the other parameterizations.

Goddard and New Goddard are two intermediate cases. The increment of the atmospheric opacity from Goddard to New Goddard responds to three factors: i) the increase of the CO_2 mixing ratio in the second scheme, i.e. from 300 ppmv to 336 ppmv, ii) a higher ozone absorption coefficient used by New Goddard in the PAR region (Sect. 3.4) and iii) the improvement of the treatment of the reduction transmission function due to CO_2 in New Goddard.

FLG experiences a similar opacity that Goddard and New Goddard, being slightly more transparent than the first scheme. These results are coherent because FLG uses the same ozone profiles that these parameterizations (Sect. 3.7) while the trace gases are disabled in the default version leading to a lower absorption.

The analysis of DIF reveals different behaviors. CAM is the scheme that experiences the lowest scattering atmosphere with 42 Wm^{-2}, followed by Goddard with 51 Wm^{-2} and RRTMG with 54 Wm^{-2}. New Goddard and FLG produce similar results with 55 Wm^{-2}.

In a dry atmosphere, there are two contributions to the light scattering: aerosols and Rayleigh. As in these experiments aerosols are neglected, the unique physical process considered is the Rayleigh scattering. The parameterization of the Rayleigh scattering depends upon the set of approximations for evaluating the radiative variables and, on the method used for approximating the RTE. The differences observed between solar parameterizations indicate that there is not a high impact of the different approximations in the case of the Rayleigh scattering.

Including water vapor in the WCS scenario produces a high effect in the GHI, as a consequence of an important attenuation of the direct beam and small variations in DIF with respect to the DCS case. It does not happen by chance because water vapor is the most important absorbent in the troposphere. Moreover, in the set of experiments presented in this chapter, water vapor is assumed in a really pessimistic case, i.e. a high water vapor mixing ratio.

Dudhia is the scheme that experiences the highest reduction due to the interaction with water vapor reaching a GHI of 1037 Wm^{-2} (-15%). CAM and RRTMG experiences a reduction of the 14% reaching GHIs of 1047 and 1041 Wm^{-2}, respectively. New Goddard is an intermediate case with 1058 Wm^{-2} (-13%). Finally, Goddard and FLG are the schemes less sensitive to the water vapor profile decreasing a 12%, i.e. 1068 and 1073 Wm^{-2}, respectively.

The scheme that experiences the highest absorption of the direct beam is the RRTMG. The DHI decreases to 987 Wm^{-2} (-15%) while DIF remains as a constant (0%). New Goddard and CAM absorbs the same portion of radiation, a 13%, reaching values of 1004 and 1007 Wm^{-2}, respectively. The first parameterization shows a low decrease of DIF (-5%) while the second scheme reaches the highest reduction (-20%). With the -12%, Goddard and FLG show a similar absorption of DHI reaching values of 1019 and 1016 Wm^{-2} and of DIF, with a reduction of the 4%.

Water vapor contributes mainly in the absorption of the direct beam explaining the different degrees of reduction in the DHI. On the contrary, this gas does not have a direct impact in the source function because the Rayleigh contribution is parameterized in terms of the dry air mass. However, H_2O has an indirect impact of the DIF results. On the on hand, the portion of radiation that can be scattered decreases layer by layer due to the absorption and, on the other hand, a fraction of the scattered light is also absorbed by this gas as it was described in Sects. 2.3 and 2.4.

The impact of clouds depends on the composition and the set of approximations used by each scheme. Thus, for the St cloud, the DHI becomes zero in all schemes and hence, the

GHI is directly the DIF. The case of the Cs cloud produces a significant reduction of the DHI compensated by an increment of the DIF that leads to higher GHI values than in the WCS scenario.

In the St scenario, Dudhia is the most transparent parameterization while FLG shows the lowest GHI (i.e. DIF) with 156 and 71 Wm^{-2}, respectively. The other schemes reach intermediate results. Goddard, New Goddard and CAM have similar values with 130, 122 and 130 Wm^{-2} whereas RRTMG has 114 Wm^{-2}.

The discussion in the Cs scenario is more complex. The lowest GHI is produced by Dudhia with 1052 Wm^{-2}, while Goddard and FLG reach 1157 and 1121 Wm^{-2}, respectively. New Goddard, CAM and RRTMG show similar results between 1081, 1088 and 1099 Wm^{-2}.

The comparison between the results for DIF in Goddard in the WCS and St scenarios shows that this scheme does not interacts with the cloud layer, as it was mentioned previously. The differences in DHI between both scenarios are produced by differences in the water vapor profile. This misrepresentation of the cloud layer is a consequence of the high threshold used for enabling the interaction with clouds. This problem was solved in New Goddard by decreasing this value as it can be observed in the results.

RRTMG experiences the highest attenuation of the direct beam with 695 Wm^{-2} but, concurrently, the highest scattering with 393 Wm^{-2}. New Goddard shows similar results with 848 and 233 Wm^{-2}, for DHI and DIF. Finally, CAM and FLG achieve similar values for DHI and DIF with 923 and 177 Wm^{-2} in CAM, and 955 and 166 Wm^{-2}, in FLG.

5.3.2 Physical discussion of the asymptotic fluxes and pprofiles

In the dry atmosphere scenario, all schemes show similar flux profiles. The direct component of the downward flux shows two different behaviors for the troposphere and for the upper atmosphere. In the first one, it follows a linear relationship with the pressure while in the upper levels it shows more complex patterns (Fig. 5.8). As aforesaid, in a dry atmosphere without aerosols, the unique contribution to the radiative transfer is given by the air molecules. In the troposphere, ozone is negligible, while the trace gases mixing ratios are assumed as a constant for each specie. The contribution of each gas at each layer is evaluated as a function of the gas mixing ratio and the dry air mass that is determined by the hydrostatic equation that is linearly related with the pressure (Eq. 2.110). Conversely, ozone is the main absorbent in the upper atmosphere. The ozone profile varies strongly with height breaking down the linear relationship observed in the troposphere.

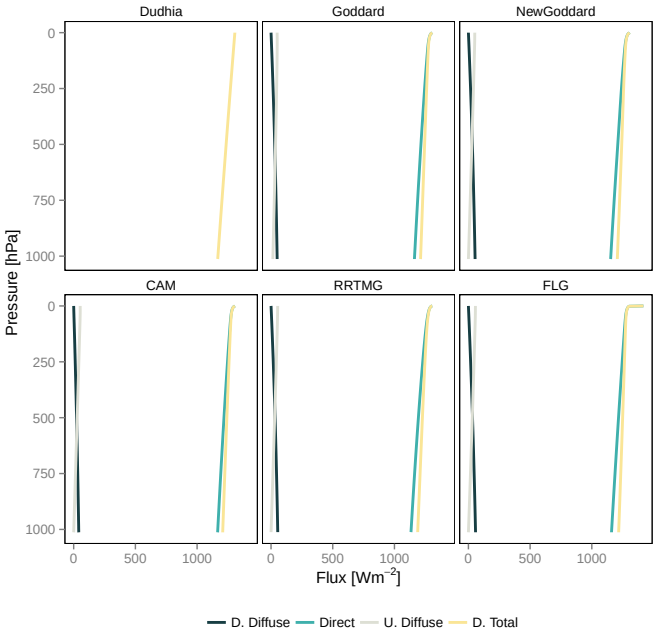

Figure 5.8: Fluxes profiles under the DCS scenario.

The downward and upward diffuse fluxes show the same order of magnitude. The first one is maximum at surface and it slowly decreases with height being zero at TOA. The other, is

maximum at TOA and becomes zero at surface because the albedo is not considered in these experiments (Sect. 5.1.2). The layer in which the downward component becomes lower than the upward one varies from one scheme to another, but it is located around 500 hPa. A similar discussion can be performed for the Rayleigh scattering leading to the observed results for the diffuse components.

As the direct component is the major component of the downward flux, the results for the total downward flux are similar to it.

Below 100 hPa, the divergence of the flux (i.e. the molecular absorption) is very low. Aside from Dudhia, FLG is the scheme that reaches the lowest heating rate (Fig. 5.9) with a mean value of 0.02 Kday^{-1} because in the implemented version the trace gasses are neglected (Fig. 3.3). Furthermore, RRTMG is the scheme that absorbs more radiation with an averaged heating rate of 0.22 Kday^{-1}. The other parameterizations show intermediate values around 0.12 Kday^{-1}.

Above 100 hPa, FLG experiences the highest absorption with an averaged heating rate of 4.78 Kday^{-1} and a maximum of 38.16 Kday^{-1} within the ozone layer. The RRTMG is the second scheme considering the absorption due to the ozone with an averaged heating rate of 3.18 Kday^{-1} and a maximum of 37.60 Kday^{-1}. Goddard, New Goddard show similar results with a mean heating rate around 2.7 Kday^{-1} and a maximum around 25 Kday^{-1}.

Dudhia produces a zero heating rate at all levels because the dry atmosphere attenuation does not contribute to the absorption parameterization given by Eq. 3.8. This is an important limitation in the stratosphere. As it was demonstrated in Montornès et al. (2015e), this simplification produces a loss of the thermal structure of the upper atmosphere that increases with the simulation horizon. Concurrently, the user's guide of the model suggests to prevent the use of this scheme for a TOM less than 50 hPa.

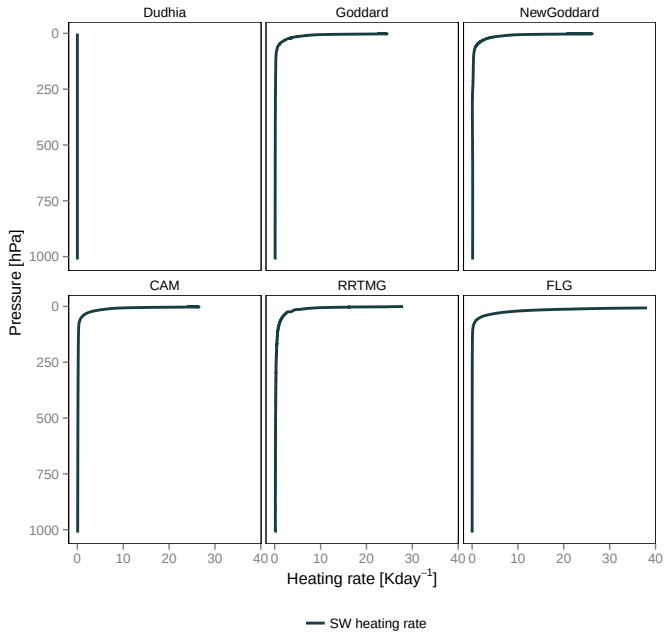

Figure 5.9: Heating rate profiles under the DCS scenario.

Water vapor produces significant changes at the lower levels (Fig. 5.12), mostly in the direct flux and hence, in the downward total flux with a high dependence on the water mixing ratio profile proposed for these experiments. The upward and downward diffuse components experience low variations with respect to the DCS case. As a consequence of the reduction of the downward flux with a conservation of the upward diffuse flux, the divergence of the flux increases producing a higher heating rate (i.e. more absorption) as it is shown in Fig. 5.13. In general, all schemes produce a similar averaged heating rate in the troposphere reducing the differences observed the dry atmosphere. CAM experiences the highest increment reaching an averaged value of 1.59 Kday^{-1} (+1225% with respect to the dry atmosphere scenario). This scheme is followed by RRTMG with 1.57 Kday^{-1} (+614%), FLG with 1.51 Kday^{-1} (+7450%), New Goddard with 1.50 Kday^{-1} (+1054%), Goddard with 1.45 Kday^{-1} (+1108%) and finally, Dudhia with

1.41 Kday^{-1} being the lowest one.

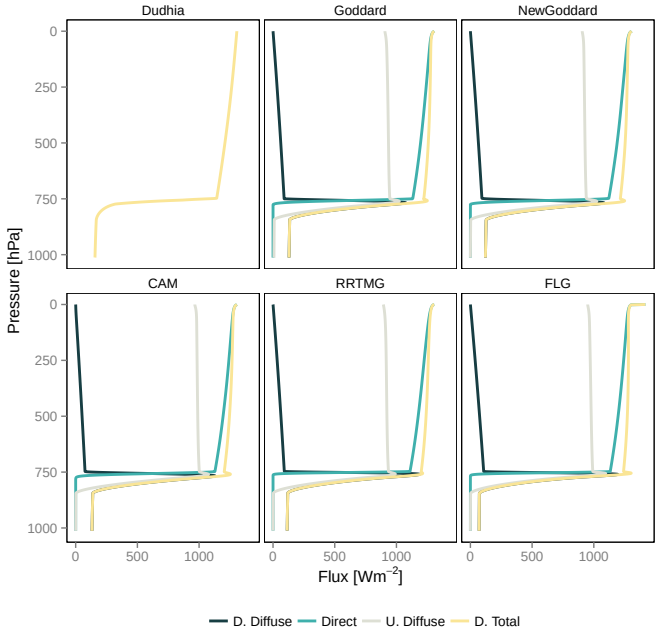

Figure 5.10: Fluxes profiles under the St scenario.

Although in the upper atmosphere water vapor is very low (Fig. 5.2), there are small differences due to the interaction with the lower levels produced by the multiscattering processes (Sect. 2.4.1). The heating rate shows small variations with respect to the DCS scenario. FLG is the scheme with the highest averaged heating rate with 5.13 Kday^{-1} (+7.3%) followed by RRTMG with 3.33 Kday^{-1} (+4.7%), New Goddard with 2.84 Kday^{-1} (+2.2%), CAM with 2.79 Kday^{-1} (+5.3%) and Goddard with 2.62 Kday^{-1} (+2.7%). Dudhia increases the averaged heating rate from 0 to 0.47 Kday^{-1} because water vapor contributes through the absorption term a_{wv} in Eq. 3.8.

The interaction between clouds and radiation has a high impact on the fluxes profiles (Figs. 5.10 and 5.11) and thus, on the heating rate profile (Figs. 5.3.2 and 5.3.2). Generally, all schemes show a similar pattern. In the region of the atmosphere above to the top of the cloud, all fluxes behave as in the WCS case with small differences due to variation in the water vapor profile. Concurrently, the upward and downward diffuse fluxes increase quickly due to the interaction with the cloud particles. Below the cloud, all fluxes recover similar patterns as those observed in the wet atmosphere scenario.

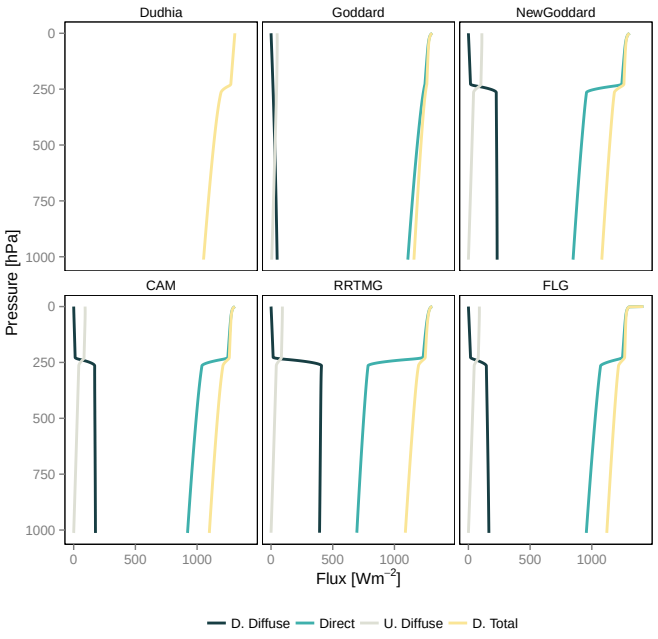

Figure 5.11: Fluxes profiles under the Cs scenario.

The impact of the cloud layer varies from one configuration to the other. For example, in the St cloud, the downward direct flux becomes zero in all schemes (i.e. the Sun is not visible at surface) as it was previously described, while in the Cs case, fluxes experience lower effects.

The absorption of the radiation produced inside the cloud lead to a quick variation of the heating rate. In the St case (Fig. 5.3.2), the scheme that produces the highest heating rate in the region between the bottom and the top of the cloud is the FLG with an averaged value of 16.4 Kday^{-1} and a peak of 70.0 Kday^{-1}. Goddard and New Goddard show similar results with an averaged heating rate of ∼13 Kday^{-1} and a maximum of 47.7 Kday^{-1} and 46.7 Kday^{-1}, respectively. The RRTMG has similar results but slightly lower with 12.7 Kday^{-1} and 46.7 Kday^{-1}. Finally, CAM is the scheme with the lowest absorption. The averaged heating rate inside the cloud is 5.7 Kday^{-1} with a peak of 17.1 Kday^{-1}.

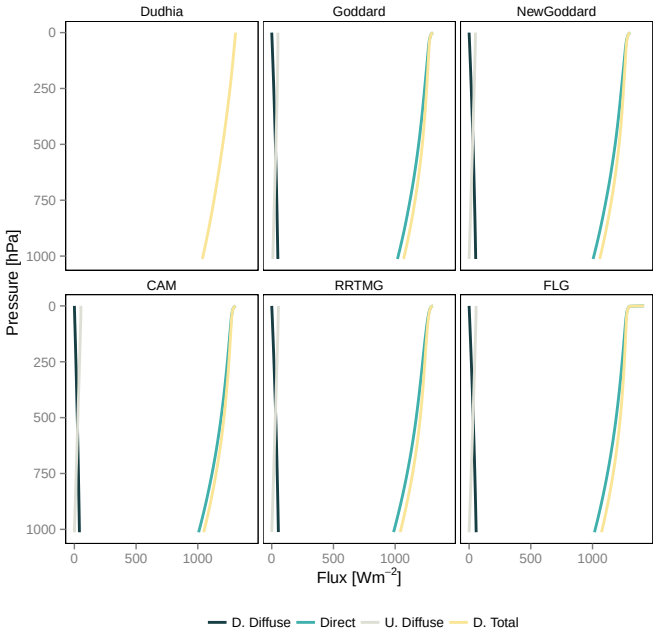

Figure 5.12: Fluxes profiles under the WCS scenario.

The Cs case experiences a similar behavior. FLG is the scheme with the highest absorption with 5.5 Kday^{-1} and a peak of 7.5 Kday^{-1} followed by New Goddard with 4.0 and 5.7 Kday^{-1}, RRTMG with 3.0 and 4.20 Kday^{-1} and, finally, CAM with 1.9 and 2.0 Kday^{-1}. As aforementioned, Goddard does not consider the cloud due to the threshold of the scheme and hence, the heating rate inside the cloud is produced only due to the peak of the water vapor profile (i.e. saturated).

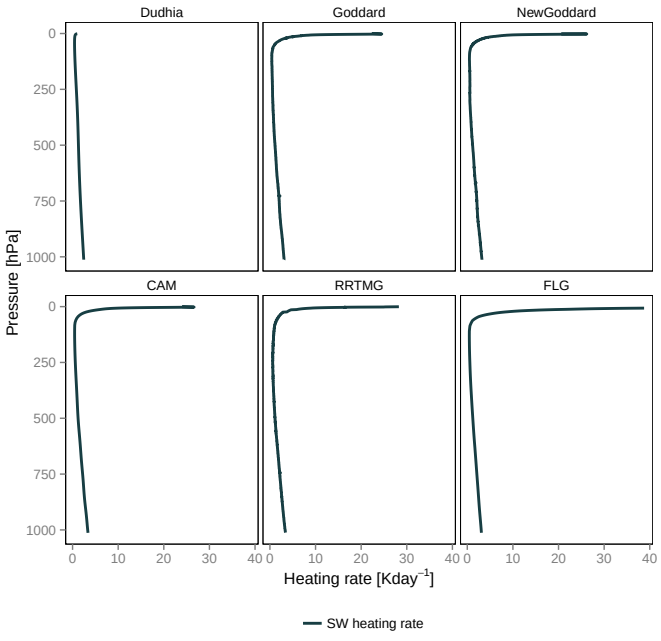

Figure 5.13: Heating rate profiles under the WCS scenario.

As Dudhia does not solve the RTE, the behavior of the downward total flux is more difficult to be compared with the others. Nevertheless, the comparison between Dudhia and the other schemes suggests that the outcome from Dudhia is more similar to the downward direct flux of the other schemes than to the total. The heating rate inside the cloud is considerably higher than in the other parameterizations. In the St case, Dudhia produces a mean value of 14.3 Kday^{-1} with a maximum of 85.2 Kday^{-1}, while in the second cloud type, these schemes show 8.3 Kday^{-1} and 12.4 Kday^{-1}, respectively.

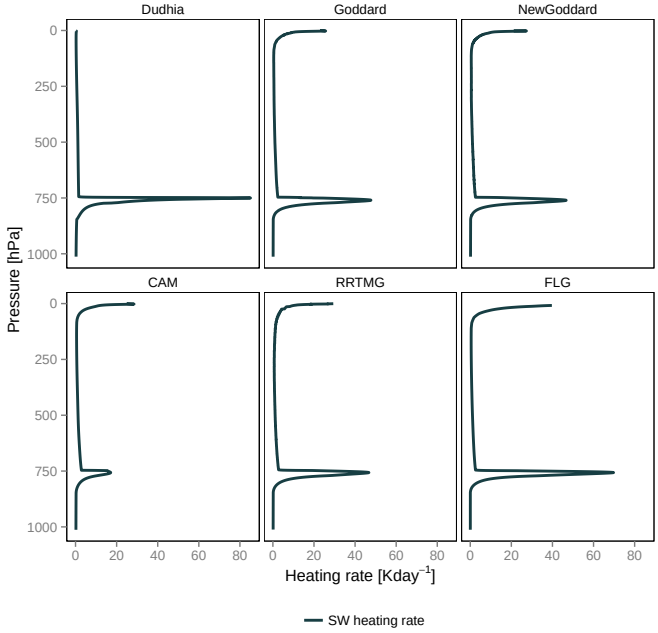

Figure 5.14: Heating rate profiles under the St scenario.

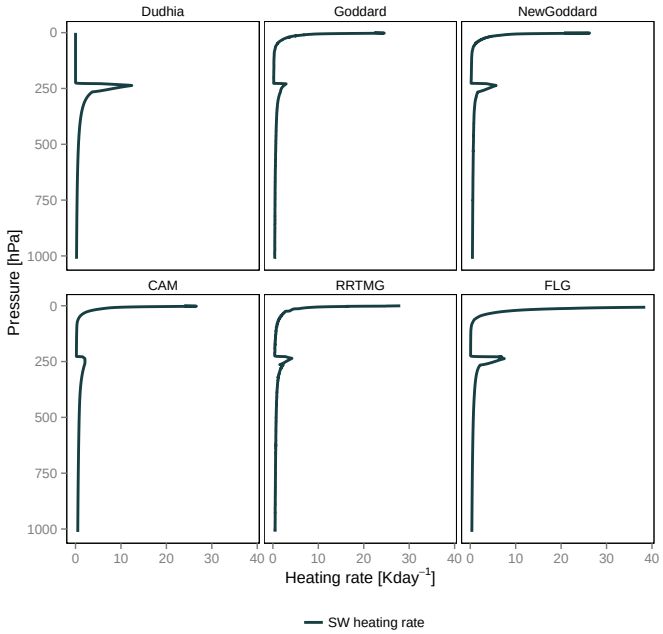

Figure 5.15: Heating rate profiles under the Cs scenario.